



High-dispersed ruthenium sites on copper phosphide/graphene for electrocatalytic hydrogen evolution in acidic and alkaline conditions

Duo Yang^{a,b}, Jing-He Yang^{c,*}, Yong-Peng Yang^{b,*}, Zhong-Yi Liu^{a,*}

^a Green Catalysis Center, and College of Chemistry, Zhengzhou University, Zhengzhou 450001, PR China

^b Henan Institute of Advanced Technology, Zhengzhou University, Zhengzhou 450052, PR China

^c School of Chemical Engineering, Zhengzhou University, Zhengzhou 450001, PR China

ARTICLE INFO

Keywords:

Copper phosphide
Electrocatalyst
Hydrogen evolution reaction
Ru single atom

ABSTRACT

Here, the novel Ru single-atomic sites (SAs) with Cu₃P nanoparticles supported on chemically converted graphene (Cu@Cu₃P-Ru/CCG) is synthesized as HER catalysts. The TEM result reveals that the average diameter of Cu@Cu₃P-Ru/CCG-500 nanoparticles (NPs) is 2 nm. AC-HAADF-STEM and Ru K-edge XAFS results uncover that the bonding environment of Ru is atomically dispersed on Cu₃P and chemically converted graphene. Cu@Cu₃P-Ru/CCG-500 exhibits a small overpotential of 32.97 mV to reach a current density of 10 mA cm⁻² (j₁₀) in 1 M KOH (102.52 mV in 0.5 M H₂SO₄). Meanwhile, its Tafel slope is 66.40 mV dec⁻¹ in 1 M KOH (63.00 mV dec⁻¹ in 0.5 M H₂SO₄). Density functional theory (DFT) calculations disclose that the Ru SAs on Cu₃P facilitate H₂O dissociation and Ru SAs on CCG promote H⁺ to form hydrogen.

1. Introduction

To achieve broad-scale hydrogen in practical application, water electrolysis could be economical, green, and efficient alternative method [1,2]. However, the hydrogen evolution reaction (HER) involves slow kinetics and high overpotential, resulting in an overmuch expenditure of energy [3,4]. Despite Pt-based noble metal materials have been accepted as the distinguished HER electrocatalyst, the reserve shortage, mono-function and high cost of Pt limit their widespread application in practical industries [5–7]. In addition, ideal HER catalysts are expected to be used in alkaline or neutral electrolyzes for the actual application [8]. The design and preparation of high-performance, earth-abundant, and pH-universal electrocatalysts for HER is an urgent need to develop the hydrogen economy [9,10].

For the past few years, transition metal phosphides (TMPs) with low-cost and high catalytic activity have been deemed promising electrocatalysts for HER [11]. Cu-based TMPs have gotten a lot of attention because of their low cost and facile preparation method. Cu-based TMPs electrocatalysts often exhibit lower catalytic activity and durability in HER [12,13]. Many reported Cu-based TMPs catalysts have poor resistance in acid media [14]. It is significance to exploit remarkable activity and durable Cu-based TMPs by designing the unique structure and regulating the sample composition [15]. To improve the catalytic

stability of these catalysts, the common strategies are to downsize the metals, anchor them on the conductive carbon-based matrix and hybridize them with other noble metals [16,17]. The bimetallic catalysts may resolve the high price and instability of HER catalysts because of the synergistic effect between diversified metal active sites [18,19]. Moreover, many reported works have established that the noble metal species usually reunite or form particles, which is unfavorable to reveal the active sites. Inspired by the agglomeration and size effect on the catalytic activity, together with the actuating force to make the best of single-atom catalysts have been deemed an ideal substitute for HER electrocatalyst [20]. The state-of-the-art SAs catalysts have shown some merit: for example, 100% metal dispersity; maximum atom utilization efficiency; the highest catalytic activity; providing the most ideal strategy to create cost-effective catalysts [21,22]. Furthermore, the SAs with especially activity centers provide the catalytic activity mechanisms at the atomic level and bring the crux challenges to the field of HER. In this regard, single atoms anchored TMPs are a perfect model to maximize the HER activity. In this work, we chose the comparatively low-budget Ru as the single atom element because its Ru-H bond strength is similar to that of Pt-H [23]. It is also a challenge to stabilize SAs on TMPs for HER in electrolytes [24]. Graphene oxide (GO) with high conductivity and high surface area is commonly used as a basement [25]. GO contributes electrons more and enhances the interaction between GO support and

* Corresponding authors.

E-mail addresses: jhyang@zzu.edu.cn (J.-H. Yang), pyyang2017@zzu.edu.cn (Y.-P. Yang), liuzhongyi@zzu.edu.cn (Z.-Y. Liu).

<https://doi.org/10.1016/j.apcatb.2023.122402>

Received 7 November 2022; Received in revised form 28 December 2022; Accepted 16 January 2023

Available online 18 January 2023

0926-3373/© 2023 Elsevier B.V. All rights reserved.

guest molecules [26,27]. These unique characteristics of GO make it to be an ideal candidate to support and stabilize SAs on TMPs catalysts [28, 29].

Herein, we successfully prepared a unique double active site structure of Ru SAs on Cu₃P and Ru SAs on CCG by treatment the RuCuPO/GO precursor in pure H₂ at high temperature. The distribution of the Cu and Ru on the surface of catalysts is greatly regulated by reduction temperatures, thereby affecting the HER activity. Benefiting from the unique double active site structure of Ru SAs on Cu₃P and Ru SAs on CCG, Cu@Cu₃P-Ru/CCG-500 NPs exhibit high HER activity and durability in alkaline and acid solution, which is verge on the commercial 20% Pt/C in the same test conditions. Cu@Cu₃P-Ru/CCG-500 NPs exhibit a small overpotential of 32.97 mV to reach j₁₀ in 1 M KOH (102.52 mV in 0.5 M H₂SO₄). Meanwhile, its Tafel slope is 66.40 mV dec⁻¹ in 1 M KOH (63.00 mV dec⁻¹ in 0.5 M H₂SO₄). This work supplies a new direction for the preparation of the double active site construction of noble metal/transition metal phosphide electrocatalysts for the practical application of electric-to-hydrogen energy conversion.

2. Experimental section

2.1. Materials

The raw materials employed in the preparation of the Cu@Cu₃P-Ru/CCG-500 NPs were Cupric nitrate (Cu(NO₃)₂·3 H₂O, ≥ 99%), Ruthenium trichloride (RuCl₃·xH₂O, Ru content 37 wt%), Graphite oxide (GO), Phosphoric acid (H₃PO₄, ≥85%), Urea(CO(NH₂)₂, ≥ 99%), Sodium dodecyl sulfate (SDS, ≥92.5%), Ethanol (C₂H₅OH, ≥99.5%), Potassium hydroxide (KOH, ≥85%), Sulfuric acid (H₂SO₄, ≥98%) and Nafion (5 wt %). The commercial Pt/C (20%) catalysts were purchased from Alfa Aesar. All the reagents were analytical grade and utilized without further purification.

2.2. Synthesis of RuCuPO/GO precursors

The RuCuPO/GO precursors were synthesized according to our previous report with small modifications [30]. Typically, Cu (NO₃)₂·3 H₂O (0.1 mM), RuCl₃·xH₂O (0.1 mM), Urea (1.2 g), SDS (0.1 g), GO (5 mg), H₃PO₄ (41 μL), and deionized water were mixed in a beaker and stirred for 30 min before hydrothermal treatment at 80 °C for 12 h. Then, the precipitate was collected by suction filtration and dried to obtain the precursor RuCuPO/GO.

2.3. Synthesis of Cu@Cu₃P-Ru/CCG-500 NPs

The as-obtained precursors RuCuPO/GO were reduced under pure H₂ (heating rate; 10 °C/min) at different temperatures (400 °C, 500 °C, 600 °C and 700 °C) for 2 h. The resulting catalysts were named as Cu@Cu₃P-Ru/CCG-400, Cu@Cu₃P-Ru/CCG-500, Cu@Cu₃P-Ru/CCG-600, and Cu@Cu₃P-Ru/CCG-700.

2.4. Synthesis of Cu@Cu₃P/CCG-500 nanosheet

The synthesis procedure for Cu@Cu₃P/CCG-500 was the same as Cu@Cu₃P-Ru/CCG-500 except that the RuCl₃·xH₂O was not added to the mixed solution.

2.5. Synthesis of Ru₂P/CCG-500 NPs

The synthesis procedure for Ru₂P/CCG-500 was the same as Cu@Cu₃P-Ru/CCG-500 except that the Cu (NO₃)₂·3 H₂O was not added to the mixed solution.

2.6. Characterizations

The morphology of the as-prepared samples was characterized by

scanning electron microscope (SEM), transmission electron microscopy (TEM), high-angle annular dark-field scanning transmission electron microscopy (HAADF-STEM) and high-resolution transmission electron microscopy (HRTEM) (FEI-Talos F200s). Ru SAs was measured by aberration-corrected high-angle annular dark-field scanning transmission electron microscopy (AC-HAADF-STEM). AC-HAADF-STEM was carried out on thermalfisher scientific titan themsis Z. The crystal structure of samples was performed by powder X-ray diffraction (Bruker AXS D8 Advanced) with Cu Kα radiation (λ = 0.15406 nm). X-ray photoelectron spectra (XPS) were performed on AXIS Supra using Al as the excitation source. Ru K-edge XAFS analyses were carried out with Si (111) crystal monochromators at the BL14W Beam line at the Shanghai Synchrotron Radiation Facility (SSRF) (Shanghai, China). The XAFS spectra were recorded using a 4-channel Silicon Drift Detector (SDD) Bruker 5040 at room temperature. Ru K-edge X-ray absorption near edge structure (XANES) and extended X-ray absorption fine structure (EXAFS) spectra were acquired in transmission mode. Raman measurements were collected with a LabRAM HR Evolution (HORIBA) instrument. Fourier transform infrared spectroscopy (FT-IR) spectra were performed on Nicolet IS10 spectrometer (American Thermo company). Inductively coupled plasma optical emission spectrometer (ICP-OES) was performed on Agilent 5110.

2.7. Electrochemical measurements

A CHI760E electrochemical workstation (Chen Hua, Shanghai, China) was used to measure the electrocatalytic activities towards HER. All electrochemical tests were performed with a three-electrode setup at room temperature, using a modification glassy carbon electrode (GCE, 3 mm diameter, 0.07065 cm²) as the working electrode, a graphite rod as the counter electrode, Hg/HgO electrode, and Hg/Hg₂SO₄ electrode as the reference electrode in alkaline and acid solution, respectively. For the fabrication of the working electrode, 5 mg of the as-prepared samples or commercial 20% Pt/C were dispersed in 1 mL 0.1% Nafion solution (5% solution, Sigma-Aldrich). The mixed solution was sonicated for 30 min to form a homogeneous ink. 10 μL of the catalyst inks were loaded onto the polished glassy carbon electrode and left to dry. All potentials were calibrated to the reversible hydrogen electrode (RHE): E_{RHE} = 0.924 V + E_{Hg/HgO} (1 M KOH); E_{RHE} = 0.652 + E_{Hg/Hg₂SO₄} (0.5 M H₂SO₄). Linear sweep voltammetry (LSV) was conducted at the scan rate of 2 mV s⁻¹. The electrochemical impedance spectroscopy (EIS) tests were executed with a frequency range from 0.1 Hz to 100 kHz at the amplitude of 5 mV. The multi-current steps were measured at the current density of -10 mA cm⁻², -30 mA cm⁻², -50 mA cm⁻², -100 mA cm⁻², -150 mA cm⁻² for 5 h. Cyclic voltammetry (CV) was conducted to calculate the double-layer capacitance (C_{dl}). CV was tested at a scan rate range of 10 mV s⁻¹ ~ 60 mV s⁻¹. The chronopotentiometry curve was recorded at j₁₀. All the polarization curves were recorded with iR compensation.

3. Results and discussion

3.1. Morphology and structural characteristics of Cu@Cu₃P-Ru/CCG-400~700

Fig. 1 illustrates the synthesis process for pure Cu@Cu₃P/CCG-500, Ru₂P/CCG-500 and Cu@Cu₃P-Ru/CCG-500. The RuCuPO/GO precursors were synthesized through a two-step procedure. First, 0.1 mM Cu (NO₃)₂·3 H₂O, urea (1.2 g), SDS (0.1 g), GO (5 mg), 0.1 mM RuCl₃·xH₂O solution and 41 μL phosphoric were dissolved in deionized water. After stirring for 30 min, the above mixture solution was kept at 80 °C for 12 h. After cooling, the samples were collected by suction filtration and washed with ethanol and water several times. The obtained samples were denoted as RuCuPO/GO. Secondly, the as-obtained RuCuPO/GO materials were treated at 500 °C under pure H₂ (heating rate: 10 °C/min) for 2 h. The acquired samples were named Cu@Cu₃P-

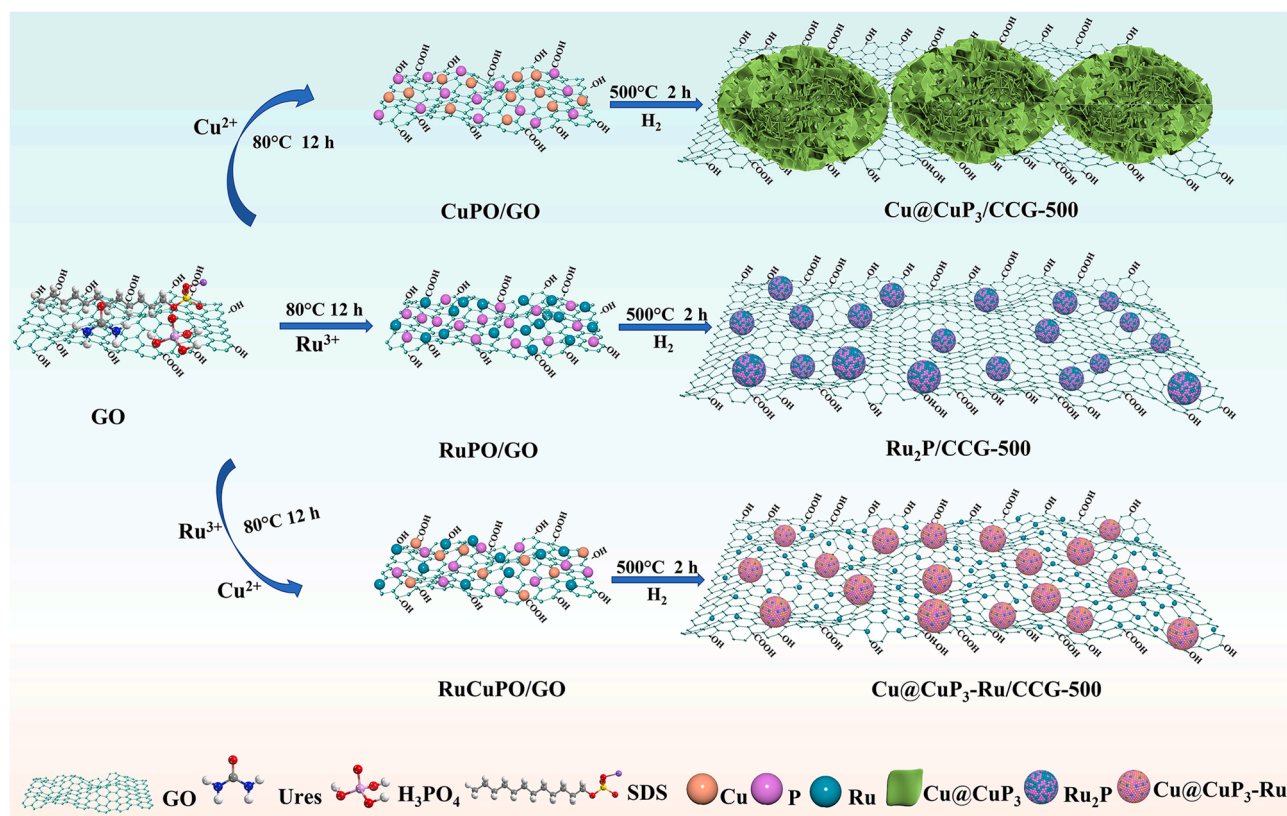


Fig. 1. Schematic illustration of the preparation of pure Cu@Cu₃P/CCG-500, Ru₂P/CCG-500 and Cu@Cu₃P-Ru/CCG-500.

Ru/CCG-500. The synthesis procedure for Cu@Cu₃P/CCG-500 was the same as Cu@Cu₃P-Ru/CCG-500 except that the RuCl₃·xH₂O was not added to the mixed solution. The synthesis procedure for Ru₂P/CCG-500 was the same as Cu@Cu₃P-Ru/CCG-500 except that the Cu (NO₃)₂·3 H₂O was not added to the mixed solution.

The XRD result (Fig. 2a) reveals that the diffraction peaks at 36.11°, 39.19°, 41.65°, 45.18°, 46.26°, 47.44°, 53.63° and 66.59° for Cu@Cu₃P/CCG-500 are indexed to (112), (022), (121), (030), (113), (122), (014) and (223) facets of standard Cu₃P (PDF No. 01–071–2261). The diffraction peaks at 43.39°, 50.51°, and 74.16° are assigned to (111), (002), and (022) facets of standard Cu (PDF No. 00–004–0836). The Cu₃P and Cu in Cu@Cu₃P-Ru/CCG-500 shifted to lower angles compared with the pure Cu@Cu₃P/CCG-500. The characteristic peaks at approximately 29.20°, 31.92° and 32.45° for Cu@Cu₃P-Ru/CCG-500 are attributed to (−2 2 2), (−2 2 3) and (4 0 1) lattice facets of Cu₂P₇ (PDF No. 01–076–1189) with the peaks shifted to lower angles. The reason for the Cu₂P₇ phase appeared is that the atomic radius of Ru is relatively large, which increases the gap of copper and promotes the embedment probability of P atom after the introduction of Ru. The Fig. S4 reveals that Ru₂P/CCG-500 is mainly constituted by Ru₂P (PDF# 03–65–2382). The XRD result caused by the implantation of Ru atoms with larger atomic radius into Cu@Cu₃P, which leads to larger crystal plane spacing, hinting the successful synthesis of Cu@Cu₃P-Ru alloy. There is no characteristic peak of Ru-related species found, insinuating that the Ru elements are highly dispersed, amorphous or sufficiently small[31]. The XRD pattern of RuCuPO/GO and Cu@Cu₃P-Ru/CCG-400–700 was displayed in Fig. S3.

To further detected the morphology of the as-prepared samples, SEM and TEM were conducted. As displayed in Fig. 2b, the SEM image of pure Cu@Cu₃P/CCG-500 shows a homogeneous interconnected quadrangle nanosheet structure with a smooth surface vertically grown on CCG. SEM image of pure Ru₂P/CCG-500 exhibits a lot of nanoparticles covered in crumpled graphene (Fig. 2c). When the introduction of Ru

atom, the image of Cu@Cu₃P/CCG-500 changed from the quadrangle nanosheet structures to nanoparticles. SEM image of Cu@Cu₃P-Ru/CCG-500 exhibits that a graphene flake-like nanosheet structure with lots of small particles was preserved after high temperature treatment under pure H₂. The synthesis procedure for Cu@Cu₃P/CCG-500 was the same as Cu@Cu₃P-Ru/CCG-500 except that the RuCl₃·xH₂O was not added to the mixed solution. The synthesis procedure for Ru₂P/CCG-500 was the same as Cu@Cu₃P-Ru/CCG-500 except that the Cu (NO₃)₂·3 H₂O was not added to the mixed solution. SEM image results imply that the morphology of the material was changed after the introduction of Ru atom (Fig. 2d). The SEM images of Cu@Cu₃P-Ru/CCG-400, Cu@Cu₃P-Ru/CCG-600 and Cu@Cu₃P-Ru/CCG-700 exhibited in Fig. S1. SEM image results imply that the morphology of control catalysts was similar with Cu@Cu₃P-Ru/CCG-500 with some monodispersed Cu@Cu₃P-Ru NPs loading on the surface of CCG film. As exhibited in Fig. 2e, the TEM image of GO shows a stratiform and smooth nanosheet structure. In contrast to pure GO, the TEM and HAADF-STEM images of Cu@Cu₃P-Ru/CCG-500 exhibit abundant monodisperse nanoparticles grown on thin CCG (Fig. 2f-h). HAADF-STEM images of Cu@Cu₃P-Ru/CCG-500 show the mean particle size mainly is 2 nm. The TEM images of Cu@Cu₃P-Ru/CCG-400, Cu@Cu₃P-Ru/CCG-600 and Cu@Cu₃P-Ru/CCG-700 showed in Fig. S2. TEM image results imply that the particle size of Cu@Cu₃P-Ru increases with the increase of reduction temperature from 400 °C to 700 °C. The HRTEM image exhibits a lattice fringe with lattice spacings of ≈ 0.23 nm, which is indexed to the (202) plane of Cu₃P (PDF No. 01–071–2261) (Fig. 2i).

To further detected the characterized element distribution of P, Cu and Ru in Cu@Cu₃P-Ru/CCG-500, EDS elemental mapping was employed (Fig. 3a-e). EDS spectra reveals that Cu and P signals are distributed across the Cu@Cu₃P-Ru/CCG-500 NPs, but Ru signals are unevenly distributed with less signal. EDS spectra also reveals that most of the Ru signals are dispersed on copper phosphide, and a small part of the Ru signals is distributed on CCG. To further confirm the distribution

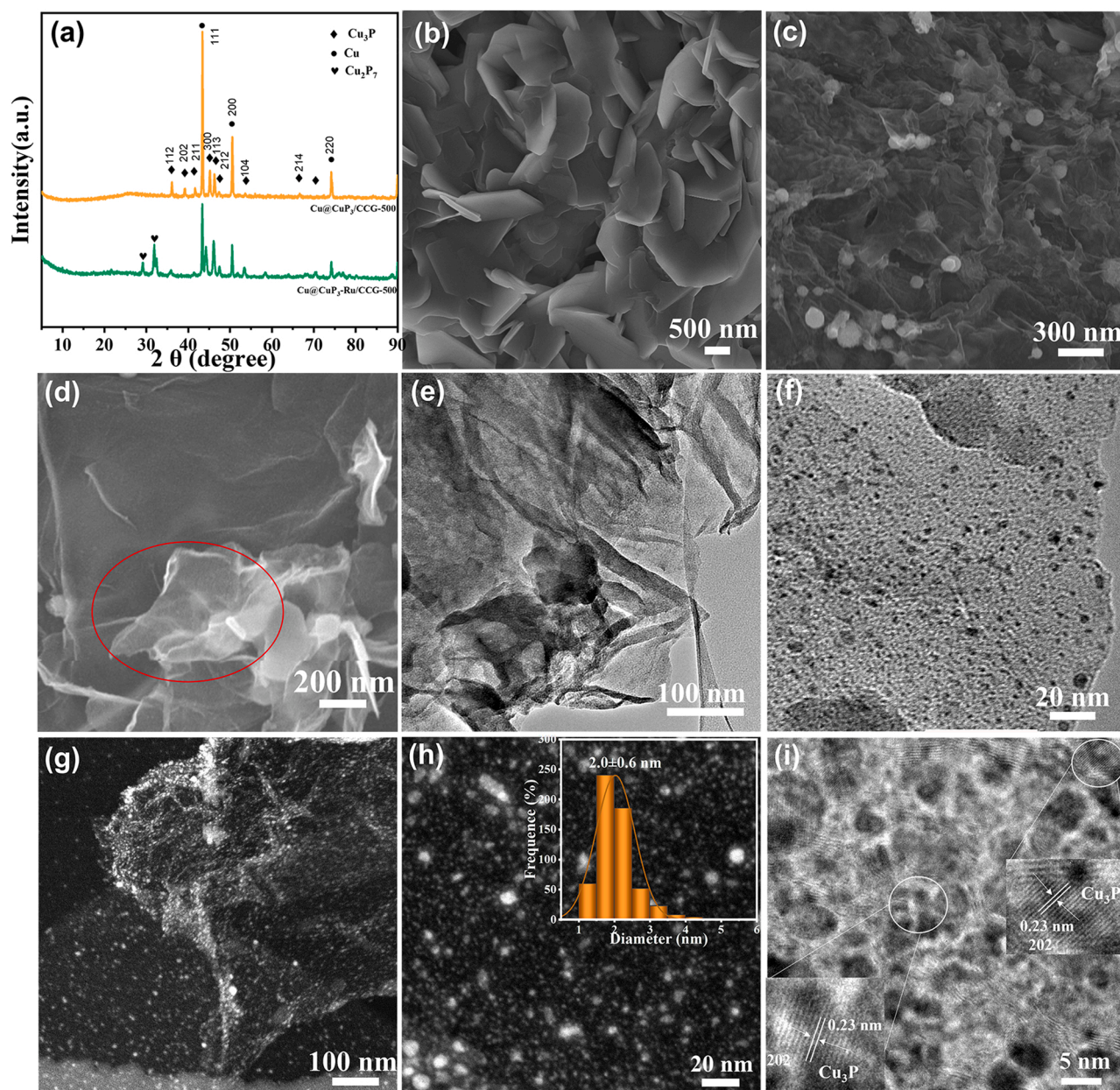


Fig. 2. (a) XRD of Cu@Cu₃P/CCG-500 and Cu@Cu₃P-Ru/CCG-500. SEM images of (b) Cu@Cu₃P/CCG-500, (c) Ru₂P/CCG-500 and (d) Cu@Cu₃P-Ru/CCG-500. TEM images of (e) GO and (f) Cu@Cu₃P-Ru/CCG-500. (g) HAADF-STEM images of Cu@Cu₃P-Ru/CCG-500. (h) Particle size distribution diagram of Cu@Cu₃P-Ru/CCG-500. (i) HRTEM images of Cu@Cu₃P-Ru/CCG-500.

of Ru elements in Cu@Cu₃P-Ru/CCG-500, AC-HAADF-STEM was conducted (Figs. 3g, 3h). It illustrates that some bright dots are anchored on Cu₃P NPs, and some other bright dots are dispersed on CCG (The bright dots circled in red are heavy Ru atoms), indicating that the existence of Ru is SAs. Moreover, EDS spectra reveals that most of the Ru signal are dispersed on copper phosphide, and a small part of the Ru signal is distributed on CCG. In addition, ICP-OES displays that the mass percentage of Ru in Cu@Cu₃P-Ru/CCG-500 NPs is 17.77%. Raman spectroscopy was used to explore the graphitization degree of carbon. As exhibited in Fig. 3i, the two characteristic peaks at approximately 1340 cm⁻¹ (D-band) and 1590 cm⁻¹ (G-band) in Cu@Cu₃P-Ru/CCG-T are observed, which are consistent with disordered and graphitic carbon. The D-band and G-band intensity ratio (ID/IG) of Cu@Cu₃P-Ru/CCG-500 is 1.05, which is similar to that of Cu@Cu₃P-Ru/CCG-400 (1.06), Cu@Cu₃P-Ru/CCG-600 (1.03) and Cu@Cu₃P-Ru/CCG-700 (1.04), indicating that the carbon composition in those samples

possesses the similar degree of disorder for sp² carbon [32].

To further determine the bonding environment of Ru in Cu@Cu₃P-Ru/CCG-500, the XANES and EXAFS was carried out. The Ru K-edge XANES profiles of absorption Cu@Cu₃P-Ru/CCG-500, Ru foil, and RuO₂ a shown in Fig. 4. The near-edge energy of Ru in Cu@Cu₃P-Ru/CCG-500 situates between Ru foil and RuO₂ in a range from 22,050 eV to 22,250 eV, indicating a cationic environment for the Ru species located between Ru⁰ and Ru⁴⁺ [33,34] (Fig. 4a). The Fourier transform EXAFS (FT-EXAFS) spectrum of Cu@Cu₃P-Ru/CCG-500 shows two peaks at about 1.78 and 2.60 Å, which are ascribed to Ru-P and Ru-Cu bonds, respectively (Fig. 4b). Ru-Ru bond is not found in the EXAFS spectrum of Cu@Cu₃P-Ru/CCG-500 compared to RuO₂ and Ru foil, demonstrating the atomically dispersed Ru sites, which is consistent with the result of AC-HAADF-STEM. Fig. 4c shows the fitted Ru K-edge EXAFS. The best-fitting result from FT-EXAFS exhibits that the Ru atoms in Cu@Cu₃P-Ru/CCG-500 fitted well with Cu@Cu₃P-Ru structure.

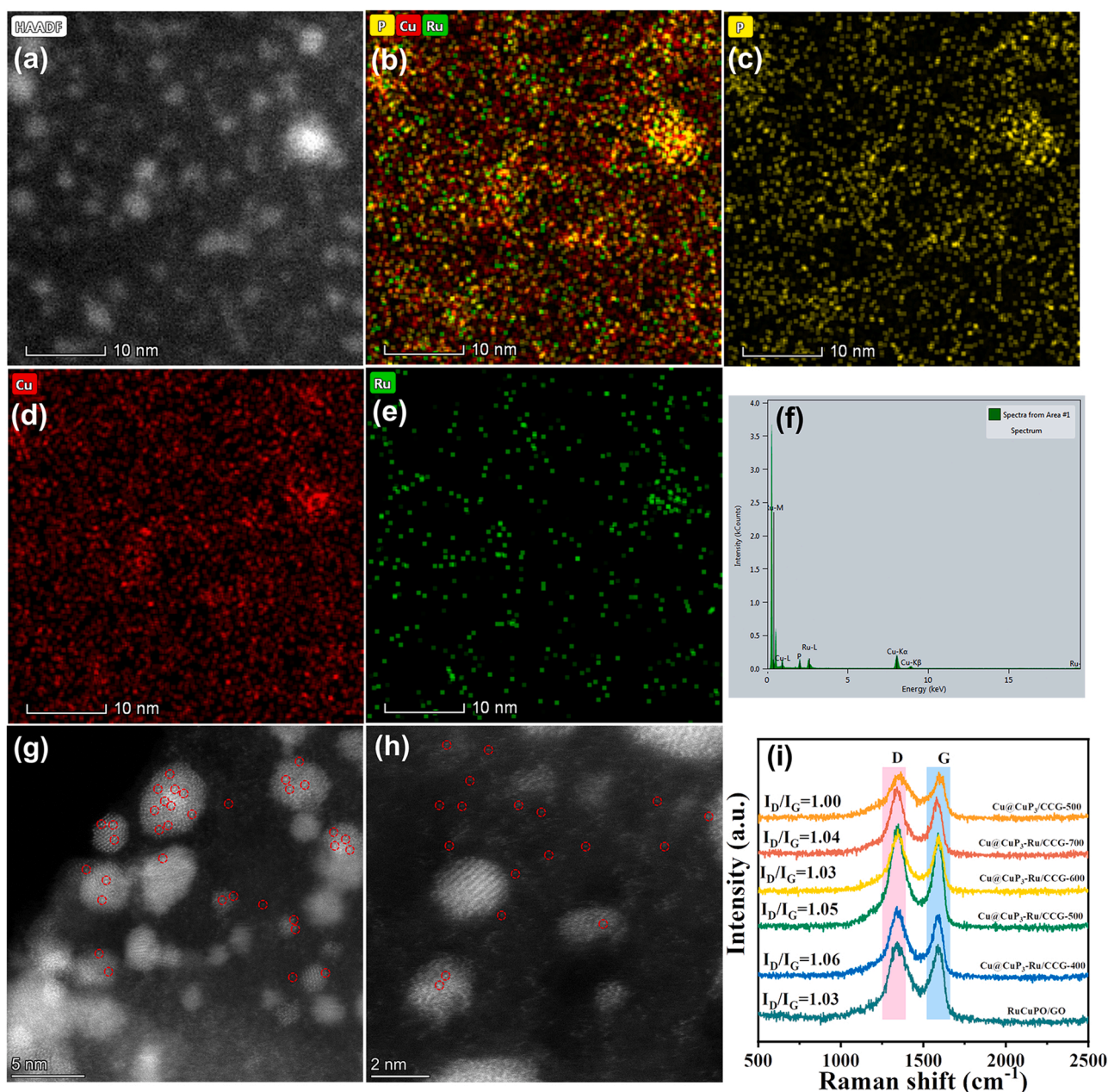


Fig. 3. (a) HAADF-STEM image of Cu@Cu₃P-Ru/CCG-500. Elemental mapping images (b) total elements, (c) P, (d) Cu, (e) Ru of Cu@Cu₃P-Ru/CCG-500. (f) Composition analysis of Cu@Cu₃P-Ru/CCG-500 based on HAADF-STEM images. (g), (h) AC-HAADF-STEM image of Cu@Cu₃P-Ru/CCG-500. (i) Raman spectra of the RuCuPO/GO, Cu@CuP₃/CCG-500 and Cu@Cu₃P-Ru/CCG-400–700.

Moreover, the wavelet transforms (WT)-EXAFS contour plot of Cu@Cu₃P-Ru/CCG-500 displays that no signals attributing to the Ru-Ru are discovered, but these signals are found in WT-EXAFS of the Ru foil and RuO₂ (Fig. 4d-e).

The XPS spectrum of the RuCuPO/GO and Cu@Cu₃P-Ru/CCG-400–700 reveals the presence of Cu, Ru, C, P, and O elements on the surface of the materials (Fig. S5). The signal of O may be originated from surface oxidation, hydroxy, or carboxyl. The predominant peak of C originates from the existence of GO in the precursor RuCuPO/GO. Fig. 5a-d exhibit the high-resolution spectrum of C 1s + Ru 3d, Ru 3p, Cu 2p and P 2p for the RuCuPO/GO and Cu@Cu₃P-Ru/CCG-400–700, respectively. As shown in Fig. 5a, the high-resolution spectrum of C 1s + Ru 3d in RuCuPO/GO displays five peaks. The peaks at 284.8, 286.51 and 288.77 eV can be ascribed to C-C, C-O, and C=O bonds, respectively. The peaks at 286.43 and 282.23 eV are attributed to Ru

3d_{3/2}, Ru 3d_{5/2}, respectively. It is significant that the binding energy of Ru 3d in Cu@Cu₃P-Ru/CCG-400–700 negatively shifts relative to that for RuCuPO/GO along with the increase of the treatment temperature from 400 °C to 700 °C, implying that the reduction temperature affected the electronic properties. For instance, the peaks at 284.79 and 280.59 eV of Ru 3d in Cu@Cu₃P-Ru/CCG-500 are assigned to Ru 3d_{3/2} and Ru 3d_{5/2}, which are lower than those of Ru 3d (286.43 and 282.23 eV) in RuCuPO/GO. This may be caused by the enhanced interaction between Cu@Cu₃P-Ru and CCG after high temperatures. As exhibited in Fig. 5b, the high-resolution spectrum of Ru 3p in RuCuPO/GO and Cu@Cu₃P-Ru/CCG-400–700 display two characteristic peaks. The characteristic peak of Ru 3p in Cu@Cu₃P-Ru/CCG-400–700 negatively shift relative to that for the precursor RuCuPO/GO. For example, the peak of Ru 3p in the precursor RuCuPO/GO (486.27 and 463.93 eV) is higher than those of Ru 3p in Cu@Cu₃P-Ru/CCG-500 (484.9 and

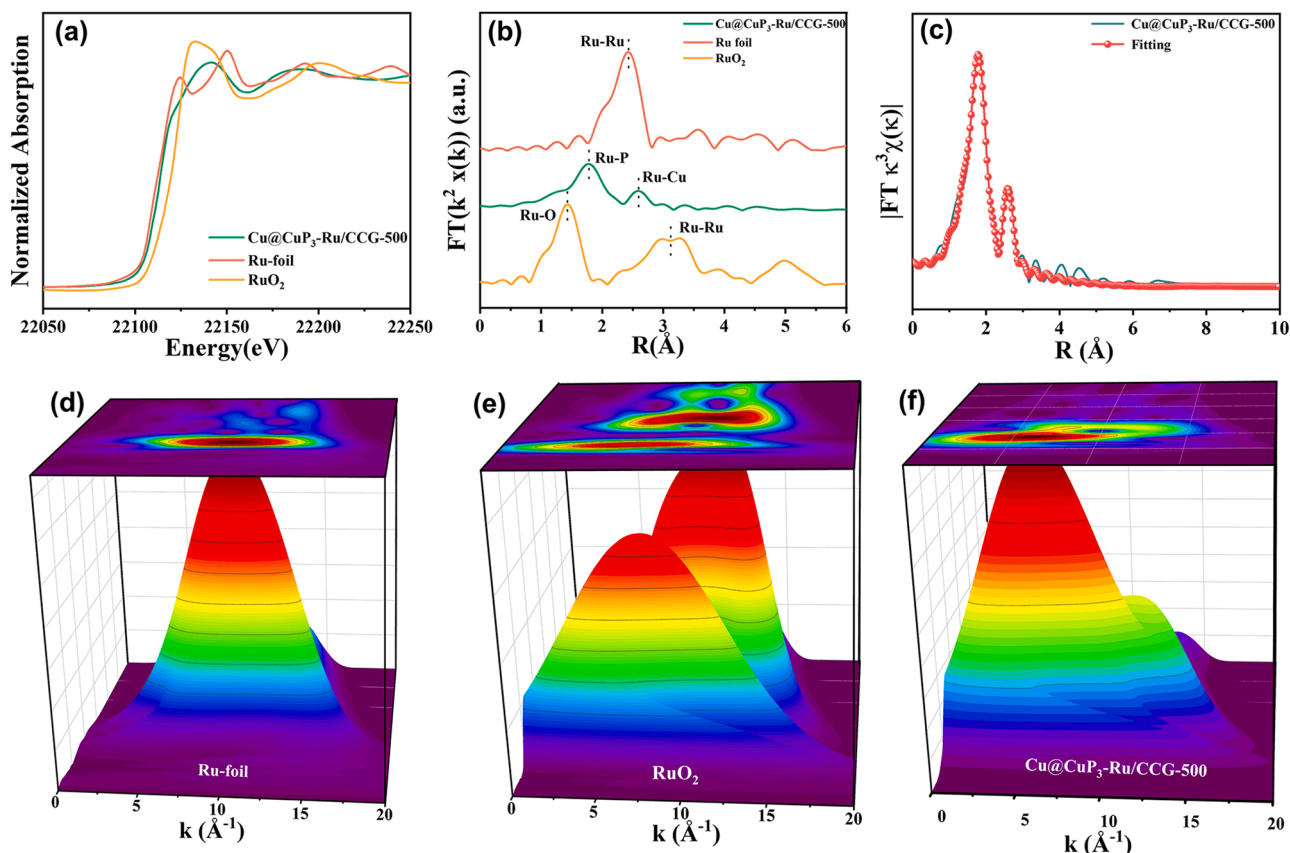


Fig. 4. (a) Ru K-edge XANES spectra and (b) the FT-EXAFS spectra of Cu@CuP₃-Ru/CCG-500, Ru foil, and RuO₂. (c) EXAFS fitting curve of Cu@CuP₃-Ru/CCG-500. (d) - (f) WT of the EXAFS spectra for Cu@CuP₃-Ru/CCG-500, Ru foil, and RuO₂.

462.26 eV). In addition, the peak of Ru 3p in Cu@Cu₃P-Ru/CCG-500 shifts toward lower binding energy compared with Ru₂P/CCG-500 (Fig. S6). This negative shift result suggests a partial electron shift from Cu₃P to Ru[35]. It is further testified by the XPS spectra of Cu 2p peaks. As exhibited in Fig. 4c, the predominant peaks of Cu 2p in Cu@Cu₃P-Ru/CCG-400–700 is divided into four. For instance, the binding energy of Cu@Cu₃P-Ru/CCG-500 at 955.64 and 935.88 eV are attributed to the Cu 2p_{1/2} and Cu 2p_{3/2}, and the binding energy at 963.20 and 943.06 eV are ascribed to the satellites. The peak of Cu 2p in the precursor RuCuPO/GO (935.18 and 955.18 eV) is lower than those of Cu 2p in Cu@Cu₃P-Ru/CCG-500 (935.88 and 955.64 eV). This result may be caused by the strong interaction between Cu@Cu₃P-Ru and CCG after high temperatures[36]. Fig. S7c displays the high-resolution spectrum of Cu 2p in pure Cu@Cu₃P/CCG-500. The two characteristic peaks are located at 952.53 and 932.72 eV, which are assigned to the Cu^{δ+} in Cu₃P[37,38]. The two characteristic peaks are located at 955.08 and 935.24 eV, which are attributed to Cu 2p_{1/2} and Cu 2p_{3/2}. The peaks at 939.04 and 943.39 eV are assigned to the satellite peaks of Cu 2p_{3/2}, and the peaks at 958.79 and 962.75 eV are attributed to the satellite peaks of Cu 2p_{1/2}[39]. Interestingly, compared with that of the pure Cu@Cu₃P/CCG-500 materials, the binding energy of Cu 2p for the Cu@Cu₃P-Ru/CCG-500 catalyst exhibited a shift to the higher binding energy. The XPS spectrum of P 2p in RuCuPO/GO precursor shows two peaks. The peaks at 134.17 and 133.30 eV are assigned to the P 2p_{3/2} and P 2p_{1/2}, respectively (Fig. 5d). The P 2p in Cu@Cu₃P-Ru/CCG-400–700 displays three peaks. For instance, the binding energy at 130.13 and 130.88 eV in Cu@Cu₃P-Ru/CCG-500 are attributed to the P 2p_{3/2} and P 2p_{1/2}, and the binding energy at 133.74 eV is attributed to P-O. It's worth noting that the binding energy of P 2p (130.13 eV) exhibits a negative shift compared with elemental P (130.2 eV) [40], suggesting that P is negatively charged (δ⁻). These

results hint that the transfer of the electron from Cu to P, in which Cu and P may act as the hydride-acceptor center and the proton-acceptor center[41].

3.2. HER performance of Cu@Cu₃P-Ru/CCG in 0.5 M H₂SO₄

The electrocatalytic performance of the as-prepared samples, as well as the commercial 20% Pt/C were evaluated in 0.5 M H₂SO₄ with a typical three-electrode system. The LSV curves for as-prepared catalysts are shown in Fig. 6a. Analogously, Cu@Cu₃P-Ru/CCG-600 and Cu@Cu₃P-Ru/CCG-700 show relatively low HER performance with a large overpotential of 150.66 mV and 196.96 mV to obtain j₁₀. In contrast, the Cu@Cu₃P-Ru/CCG-400 exhibits a moderate HER activity with a small overpotential of 105.11 mV to reach j₁₀. The Cu@Cu₃P-Ru/CCG-500 shows splendid HER activity with a low overpotential of 102.52 mV to achieve j₁₀. As anticipated, commercial 20% Pt/C displays the highest catalytic activity with an overpotential of 63.33 mV to obtain j₁₀. In addition, the overpotential value at j₁₀ of Cu@Cu₃P-Ru/CCG-500 is 102.52 mV, much lower than that of pure Cu@Cu₃P/CCG-500 (452.87 mV) and pure Ru₂P/CCG-500 (143.19 mV), which proved the facilitation role of Ru SAs incorporation in HER activity in 0.5 M H₂SO₄ (Fig. S8a). For further study the mass activity of the Cu@Cu₃P-Ru/CCG-400–700 and commercial 20% Pt/C, the current density of LSV curves of these catalysts was normalized by the mass loading in 0.5 M H₂SO₄ (Fig. 6b). It explicitly displays that the mass activity of the Cu@Cu₃P-Ru/CCG-500 was 13.23 mA mg⁻¹ over Cu@Cu₃P-Ru/CCG-400 (11.89 mA mg⁻¹), Cu@Cu₃P-Ru/CCG-600 (3.35 mA mg⁻¹) and Cu@Cu₃P-Ru/CCG-700 (1.58 mA mg⁻¹) at an overpotential of 100 mV. For further study the specific activities of the as-prepared catalysts, the LSV curves of Cu@Cu₃P-Ru/CCG-400–700 was normalized by electrochemical surface area (ECSA) in 0.5 M H₂SO₄

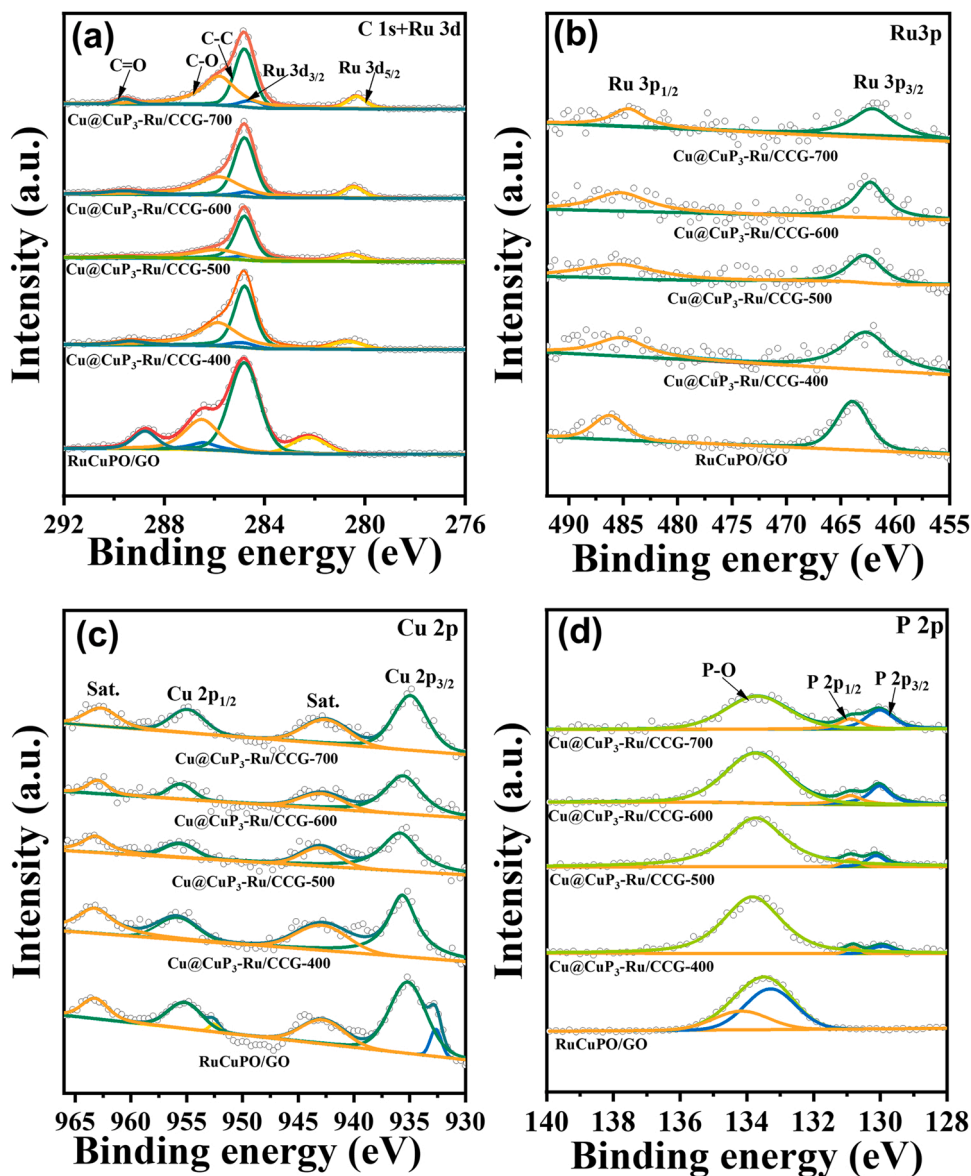


Fig. 5. High-resolution XPS spectra of (a) C 1s + Ru 3d, (b) Ru 3p, (c) Cu 2p and (d) P 2p of the RuCuPO/GO and Cu@Cu₃P-Ru/CCG-400–700.

(Fig. S9)[42]. The specific activities of Cu@Cu₃P-Ru/CCG-500 were higher than the control catalysts in the whole voltage window, indicating that Cu@Cu₃P-Ru/CCG-500 have a higher intrinsic per-site activity[43].

Theoretically, the Tafel slope is one of the important kinetic parameters to determine a reaction that occurs on the surface of the electrode. To further reveal the HER mechanism, the Tafel slopes are depicted in Fig. 6c. The Tafel slope of Cu@Cu₃P-Ru/CCG-500 is 63.00 mV dec⁻¹, which is smaller than those of Cu@Cu₃P-Ru/CCG-400 (65.42 mV dec⁻¹), Cu@Cu₃P-Ru/CCG-600 (82.40 mV dec⁻¹) and Cu@Cu₃P-Ru/CCG-700 (87.13 mV dec⁻¹), suggesting that the fast kinetics process is completed for Cu@Cu₃P-Ru/CCG-500 in HER[44–46]. Based on Volmer-Heyrovsky theory, the reaction mechanisms are related to the Tafel value, the Volmer reaction (Tafel slope > 120 mV dec⁻¹), the Heyrovsky reaction (40 mV dec⁻¹ < Tafel slope < 120 mV dec⁻¹), and the Tafel reaction (Tafel slope < 30 mV dec⁻¹)[47]. The Tafel value (63.00 mV dec⁻¹) of Cu@Cu₃P-Ru/CCG-500 indicates that the reaction process of Cu@Cu₃P-Ru/CCG-500 follows the Volmer-Heyrovsky[48,49]. To further characterize the internal resistivity and conductivity of Cu@Cu₃P-Ru/CCG-500 electrocatalysts, the EIS tests were conducted. What is more, it has been reported that the R_{ct} is the

critical factor for the impedance of cathode cells, resolving the electrochemical activity. As illustrated in Fig. 6d, the R_{ct} value of Cu@Cu₃P-Ru/CCG-500 is about 73.43 Ω , which is smaller than that of Cu@Cu₃P-Ru/CCG-400 (110.95 Ω), Cu@Cu₃P/CCG-500 (132.90 Ω) and Ru₂P/CCG-500 (217.67 Ω), and slightly larger than that of Cu@Cu₃P-Ru/CCG-600 (61.59 Ω) and Cu@Cu₃P-Ru/CCG-700 (62.92 Ω), hinting the fast electron transfer for HER[50–52].

The overpotentials for Cu@Cu₃P-Ru/CCG-400–700%, and 20% Pt/C are displayed in Fig. 6e. The acid HER activity of Cu@Cu₃P-Ru/CCG-500 is also compare with those of reported catalyst materials (Table S2). Additionally, the ECSA could be determined by the C_{dl} . The C_{dl} of Cu@Cu₃P-Ru/CCG-500 is 9.06 mF cm⁻², which is larger than those of Cu@Cu₃P-Ru/CCG-400 (8.99 mF cm⁻²), Cu@Cu₃P-Ru/CCG-600 (7.63 mF cm⁻²) and Cu@Cu₃P-Ru/CCG-700 (6.15 mF cm⁻²) (Fig. 6f and Fig. S12). This result indicates a high exposure of the active sites due to the novel double active site construction of Ru SAs on Cu₃P and Ru SAs on CCG. The Cu@Cu₃P-Ru/CCG-500 have high TOF values of 0.096, 0.55 and 2.97 s⁻¹ at overpotentials of 50, 100 and 150 mV in 0.5 M H₂SO₄, suggesting remarkable H₂ productivity (Fig. 6g)[53]. Fig. 6h exhibits the comparison of both kinetics (Tafel slope) and activity (the overpotential at 10 mA cm⁻²), indicating that

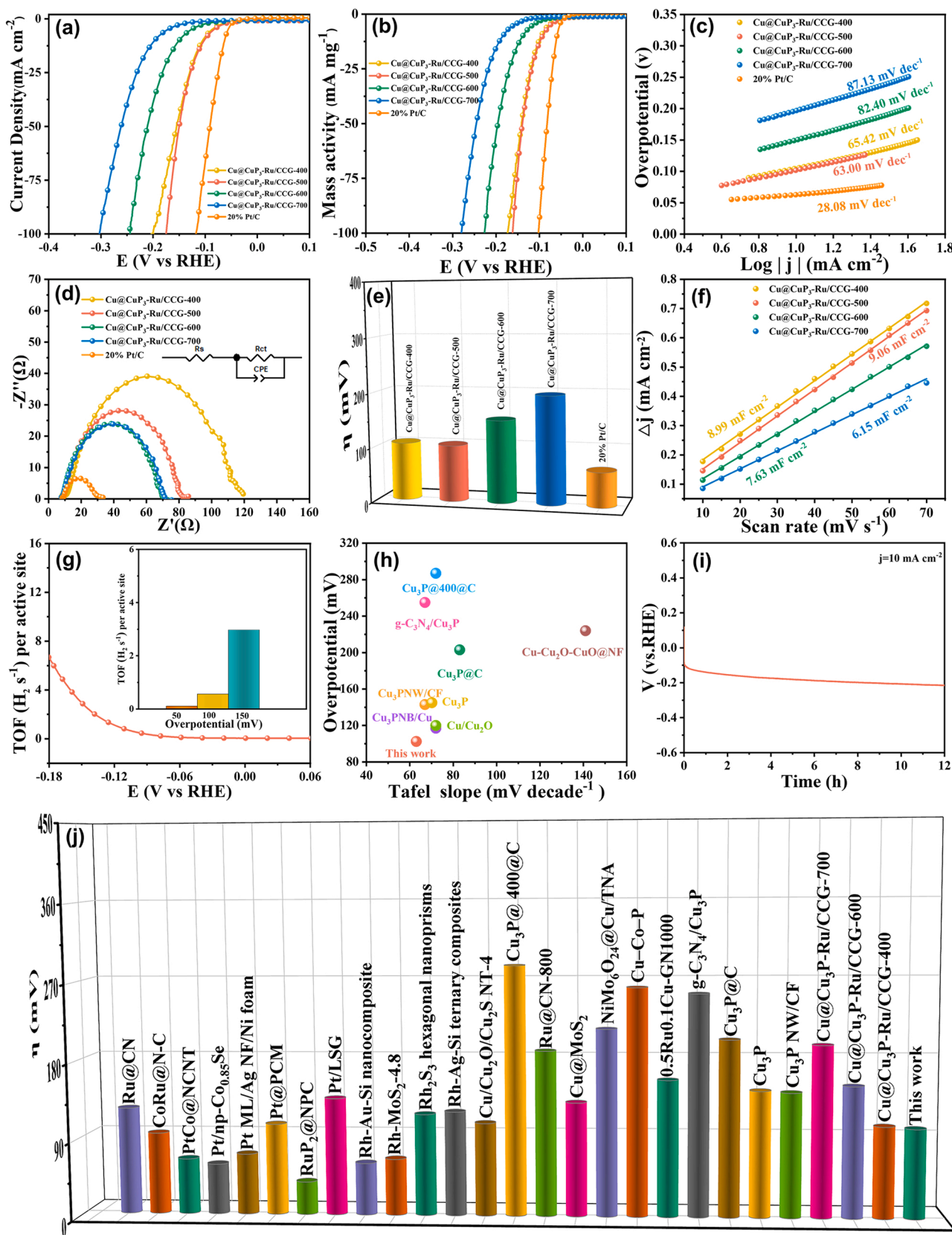


Fig. 6. (a), (b) LSV curves, (c) Tafel plots, (d) Nyquist plots, (e) Overpotentials at $j = 10 \text{ mA cm}^{-2}$ of Cu@Cu₃P-Ru/CCG-400–700% and 20% Pt/C. (f) C_{dl} of Cu@Cu₃P-Ru/CCG-400–700. (g) TOF values of Cu@Cu₃P-Ru/CCG-500. (h) Comparison of both kinetics (Tafel slope) and activity (the overpotential at 10 mA cm^{-2}). (i) Chronopotentiometry of Cu@Cu₃P-Ru/CCG-500 in 0.5 M H₂SO₄. (j) Overpotentials at 10 mA cm^{-2} of Cu@Cu₃P-Ru/CCG-500 and the reported references.

Cu@Cu₃P-Ru/CCG-500 has a good HER performance. Furthermore, the durable stability was further tested to evaluate the HER performance in 0.5 M H₂SO₄. The chronopotentiometry measurement of Cu@Cu₃P-Ru/CCG-500 at j_{10} was found that possessed about 100 mV difference before and after 12 h, which is explicit testimony that Cu@Cu₃P-Ru/CCG-500 suffers slight degradation (Fig. 6i). The catalytic activity of Cu@Cu₃P-Ru/CCG-500 was also compared with among these Cu-based and noble metal based HER catalysts at j_{10} (Fig. 6j).

3.3. HER performance of Cu@Cu₃P-Ru/CCG in 1 M KOH

Furthermore, HER activity was further estimated in 1 M KOH. As illustrated in Fig. 7a, the commercial 20% Pt/C electrocatalyst displays the highest HER activity. For the as-synthesized samples, Cu@Cu₃P-Ru/CCG-500 shows excellent HER activity with a small overpotential of 32.97 mV to reach j_{10} . In sharp contrast, the overpotential value at j_{10} of Cu@Cu₃P-Ru/CCG-500 is 32.97 mV, much lower than pure Cu@Cu₃P/

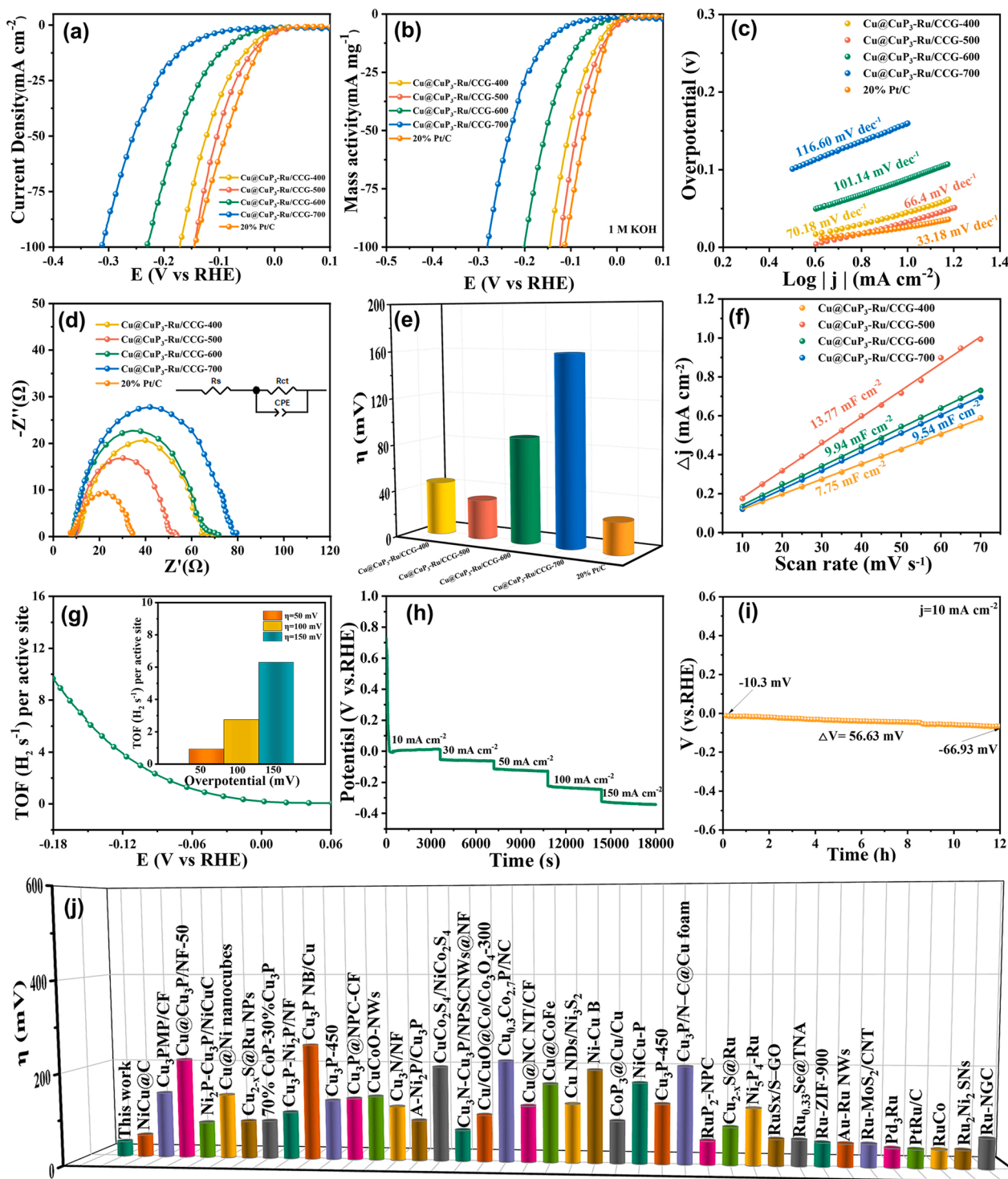


Fig. 7. (a), (b) LSV curves, (c) Tafel plots, (d) Nyquist plots, (e) Overpotentials at 10 mA cm⁻² of Cu@Cu₃P-Ru/CCG-400–700% and 20% Pt/C. (f) C_{dl} of Cu@Cu₃P-Ru/CCG-400–700. (g) TOF values of Cu@Cu₃P-Ru/CCG-500. (h) Multi current steps of Cu@Cu₃P-Ru/CCG-500 in 1 M KOH. (i) Chronopotentiometry of Cu@Cu₃P-Ru/CCG-500 in 1 M KOH. (j) Overpotentials at 10 mA cm⁻² of Cu@Cu₃P-Ru/CCG-500 and reported references.

CCG-500 (466.92 mV) and pure Ru₂P/CCG-500 (36.27 mV), this consequence testified the facilitation role of Ru SAs incorporation in HER activity in 1 M KOH (Fig. S10). The overpotential value at j_{10} of Cu@Cu₃P-Ru/CCG-500 is also lower than Cu@Cu₃P-Ru/CCG-400 (45.35 mV), Cu@Cu₃P-Ru/CCG-600 (88.79 mV) and Cu@Cu₃P-Ru/CCG-700 (159.58 mV), suggesting the reduction temperature has a great influence on HER activity. The mass activity of the Cu@Cu₃P-Ru/CCG-400–700 and commercial 20% Pt/C were further study in 1 M KOH (Fig. 7b). The mass activity of the Cu@Cu₃P-Ru/CCG-500 was 65.70 mA mg⁻¹ over Cu@Cu₃P-Ru/CCG-400 (47.72 mA mg⁻¹), Cu@Cu₃P-Ru/CCG-600 (18.20 mA mg⁻¹) and Cu@Cu₃P-Ru/CCG-700 (4.39 mA mg⁻¹) at overpotential of 100 mV. The specific activities of the as-prepared catalysts were studied in 1 M KOH (Fig. S11). The specific activities of Cu@Cu₃P-Ru/CCG-500 was lower than Cu@Cu₃P-Ru/CCG-400, but the stability of Cu@Cu₃P-Ru/CCG-400 was disappointing.

The Tafel slopes of as-synthesized catalysts were derived from LSV curves to further explain the kinetic mechanism for HER (Fig. 7c). The Tafel slopes of Cu@Cu₃P-Ru/CCG-500 (66.40 mV dec⁻¹) are higher than that of the commercial 20% Pt/C (33.18 mV dec⁻¹), but which is smaller than that of the Cu@Cu₃P-Ru/CCG-400 (70.18 mV dec⁻¹), Cu@Cu₃P-Ru/CCG-600 (101.14 mV dec⁻¹) and Cu@Cu₃P-Ru/CCG-700 (116.60 mV dec⁻¹). Significantly, the Tafel slopes of the Cu@Cu₃P-Ru/CCG-500 (66.40 mV dec⁻¹) lie between 40 mV dec⁻¹ and 120 mV dec⁻¹. This result hints that the reaction process of Cu@Cu₃P-Ru/CCG-500 involves the Volmer-Heyrovsky sequence[54,55]. It means that the Heyrovsky step is the rate-determining step of the reaction, and this behavior is semblable to that of the transition metal phosphide catalyst often reported. This low Tafel slope value of Cu@Cu₃P-Ru/CCG-500 indicates a faster electron transfer rate for HER[56,57]. To investigate electrocatalytic kinetics, the EIS was further utilized to analyze HER. Fig. 7d reveals that the small R_{ct} value of Cu@Cu₃P-Ru/CCG-500 is about 39.99 Ω , demonstrating a faster HER rate at between electrode and electrolyte interfaces[58,59]. Larger R_{ct} values were also calculated for Cu@Cu₃P-Ru/CCG-400 (53.83 Ω), Cu@Cu₃P-Ru/CCG-600 (54.48 Ω), Cu@Cu₃P-Ru/CCG-700 (66.68 Ω), Cu@Cu₃P/CCG-500 (205.20 Ω) and Ru₂P/CCG-500 (42.87 Ω), which resulted in lower conductivity and poorer HER activity. Cu@Cu₃P-Ru/CCG-500 electrode indicates the lowest R_{ct} and fastest HER rate, which is consistent with the results of the Tafel slope and LSV analysis. The overpotential at j_{10} was calculated to estimate the HER activity of the catalysts (Fig. 7e).

The ECSA was investigated by the C_{dl} via the linear slope of current densities and the scan rates in CV tests (Fig. S13) at different scan rates in a non-faradic potential range. As displayed in Fig. 7f, the C_{dl} value of Cu@Cu₃P-Ru/CCG-500 (13.77 mF cm⁻²) is larger than that of Cu@Cu₃P-Ru/CCG-400 (7.75 mF cm⁻²), Cu@Cu₃P-Ru/CCG-600 (9.94 mF cm⁻²) and Cu@Cu₃P-Ru/CCG-700 (9.54 mF cm⁻²), respectively. This result hints that the novel double active site construction of Ru SAs on Cu₃P and Ru SAs on CCG could exhibit abundant active sites, which is contribute to the superior HER activity. The TOF values are calculated to be about 0.92, 2.74 and 6.29 s⁻¹ for the Cu@Cu₃P-Ru/CCG-500 at overpotentials of 50, 100 and 150 mV in 1 M KOH (Fig. 7g). As illustrated in Fig. 7h, the multi-current steps curve for Cu@Cu₃P-Ru/CCG-500 with current density changing from 10 to 150 mA cm⁻² was tested. The potential remains hardly unchanged with the current density changing from 10 to 50 mA cm⁻². When the current density maintains at 100 mA cm⁻² and 150 mA cm⁻², the potential remains slightly decreased. This result indicates that the catalysts have excellent stability. Furthermore, the long-term stability was further tested to evaluate the HER performance. As illustrated in Fig. 7i, the chronopotentiometry measurement of Cu@Cu₃P-Ru/CCG-500 with a constant current density of 10 mA cm⁻² was carried out in 1 M KOH. It is found that the Cu@Cu₃P-Ru/CCG-500 possessed about.

56.63 mV difference before and after 12 h, which is explicit testimony that Cu@Cu₃P-Ru/CCG-500 scarcely suffers degradation. The good catalytic activity of Cu@Cu₃P-Ru/CCG-500 was also proved by the

smallest overpotentials of 32.97 mV at j_{10} among these Cu-based and noble metal based HER catalysts (Fig. 7j). The alkaline HER activity of Cu@Cu₃P-Ru/CCG-500 is also compare with those of reported catalyst materials (Table S3). To further probe the durability of the Cu@Cu₃P-Ru/CCG-500, the XRD pattern, XPS spectra and TEM image of Cu@Cu₃P-Ru/CCG-500 were executed after the chronopotentiometry test. The XRD pattern of the Cu@Cu₃P-Ru/CCG-500 remains unchanged except the peak of substrate (FTO) (Fig. S14). The peak at 21.42°, 35.31° and 30.30°, 60.27° are assigned to the SiO₂ (PDF No. 01–076–0934) and SiO₂ (PDF No. 01–071–0649). Furthermore, the XPS spectra of the Cu@Cu₃P-Ru/CCG-500 have no obvious changes after chronoamperometry test (Fig. S15). The intensity of C=O increase after stability test reveals the existence of oxidation on the surface of the catalyst. In addition, the Cu^{δ+} appears in Cu 2p of Cu@Cu₃P-Ru/CCG-500 after stability test. The TEM result reveals that the morphology of the Cu@Cu₃P-Ru/CCG-500 was partially reunited after chronoamperometry test (Fig. S16).

3.4. DFT calculation

To uncover the influence of the novel double active site construction of Ru SAs on Cu₃P and Ru SAs on CCG on HER activity, DFT calculations were conducted. The structures of pure Cu₃P, Cu₃P with Ru SAs incorporation (Ru₁-Cu₃P), and CCG with Ru SAs incorporation (Ru₁P₄) were established. Firstly, we calculated the reaction pathway of water splitting to form hydrogen. The reactant, transient state and product surface models of water splitting for Cu₃P, Ru₁-Cu₃P and Ru₁P₄ are shown in Fig. 8a-c. Fig. 8d exhibits the H₂O dissociation energy barrier. The calculations result shown that the H₂O dissociation energy barrier on Ru₁-Cu₃P is 1.01 eV, which is smaller than that of Cu₃P (1.65 eV) and Ru₁P₄ (1.72 eV), suggesting that the reaction of the H₂O dissociation on Ru₁-Cu₃P is easier than Cu₃P and Ru₁P₄. Then, we calculated the reaction pathway of H adsorbed on Ru atom reacts with water to form hydrogen. The reactant, transient state and product surface models of water splitting for Cu₃P, Ru₁-Cu₃P and Ru₁P₄ are shown in Fig. 8e-g. As exhibited in Fig. 8e-g, the H adsorbed on Cu₃P and the H adsorbed on Ru₁-Cu₃P reacts with water to form hydrogen in transient state, and the H adsorbed on Ru₁P₄ reacts with water to form hydrogen in final state. As exhibited in Fig. 8h, the calculated reaction energy barriers verified that the reaction barrier of the adsorbed H on Ru atom reacts with H₂O to form H₂ on Ru₁P₄ (0.74 eV) is the smaller than that of Cu₃P (1.02 eV) and Ru₁-Cu₃P (0.99 eV), suggesting that adsorbed H reacts with H₂O to form H₂ on Ru₁P₄ is easier than Cu₃P and Ru₁P₄. In a word, DFT calculations reveal that the Ru SAs on Ru₁-Cu₃P facilitate H₂O dissociation and Ru SAs on CCG promote H* to form hydrogen.

The projected density of states is shown in Fig. 8i. It is found that the 4d + 5s states of Ru in Ru₁-Cu₃P near Fermi level are continuous from - 8–2 eV. They are closer to the Fermi level than those of Cu, suggesting that the superior activity of Ru compared with Cu. On the other hand, the 4d + 5s states of Ru in Ru₁P₄ shift to lower energy, as low as - 10 eV, resulting in that the adsorption of reactants on Ru is weakened (Fig. 8j). For example, the H adsorption on Ru in Ru₁P₄ is lower than that of Ru in Ru₁-Cu₃P by 0.59 eV, which is beneficial for hydrogen desorption. The different electron density is shown in Fig. S17, the red and yellow regions represent the electron accumulation and depletion, respectively. The single Ru atom gains electrons from nearby atoms for both Ru₁P₄ and Ru₁-Cu₃P, and which are 0.11 e and 0.12 e, respectively, according to Bader charge analysis.

4. Conclusions

In summary, we constructed a novel double active site construction of Ru SAs on Cu₃P and Ru SAs on CCG and evaluated the HER performance in alkaline and acid solution. Benefiting from the unique structure and component advantage, such as high electrical conductivity, abundant exposed double active site, and conductive metal Cu and Ru,

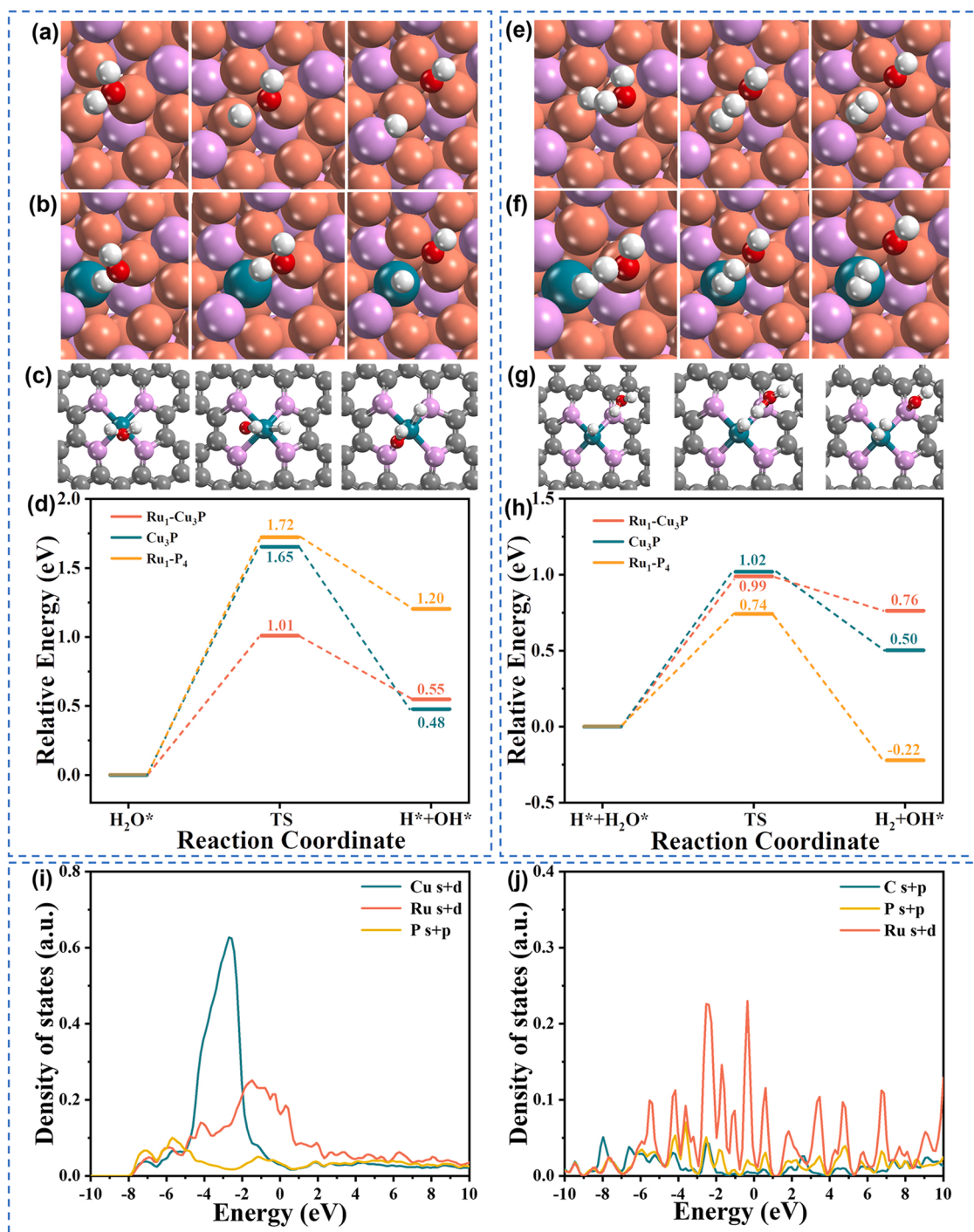


Fig. 8. (a)–(c) The top view of H_2O dissociation for Cu_3P , $\text{Ru}_1\text{-Cu}_3\text{P}$ and $\text{Ru}_1\text{-P}_4$. (d) Relative energy of the HER proceeding for Cu_3P , $\text{Ru}_1\text{-Cu}_3\text{P}$ and $\text{Ru}_1\text{-P}_4$. (e)–(g) The top view of H_2O dissociation for Cu_3P , $\text{Ru}_1\text{-Cu}_3\text{P}$ and $\text{Ru}_1\text{-P}_4$. (h) Relative energy of the HER proceeding for Cu_3P , $\text{Ru}_1\text{-Cu}_3\text{P}$ and $\text{Ru}_1\text{-P}_4$. (i) The density of states (DOS) of $\text{Ru}_1\text{-Cu}_3\text{P}$. (j) The density of states (DOS) of $\text{Ru}_1\text{-P}_4$.

$\text{Cu@Cu}_3\text{P-Ru/CCG-500}$ NPs display remarkable performance close to the commercial 20% Pt/C. As a highly conductive substrate, lamellar CCG prevents $\text{Cu@Cu}_3\text{P-Ru}$ NPs from agglomerating, exposes more active sites, and improves charge transfer rates. In return, $\text{Cu@Cu}_3\text{P-Ru}$ NPs acting as an etching agent, prompt the CCG nanosheets thinner and flatter, thereby promoting reactant supply in time and gas release fast. Impressively, $\text{Cu@Cu}_3\text{P-Ru/CCG}$ NPs exhibit a small overpotential of 32.97 mV to reach j_{10} in 1 M KOH (102.52 mV in 0.5 M H_2SO_4). Meanwhile, its Tafel slope is 66.40 mV dec^{-1} in 1 M KOH (63.00 mV dec^{-1} in 0.5 M H_2SO_4). $\text{Cu@Cu}_3\text{P-Ru/CCG}$ also display a negligible

decay after 12 h chronopotentiometry test. Density functional theory (DFT) calculations disclose that the Ru SAs on Cu_3P facilitate H_2O dissociation and Ru SAs on CCG promote H^* to form hydrogen. This work not only exploits a novel and simple method for preparing single atoms anchored TMPs to maximize the HER activity but also enlightens the application of single atom catalysts for the commercial water splitting process.

CRediT authorship contribution statement

Duo Yang: Verification, Formal analysis, Data curation, Writing – original draft. **Jing-He Yang:** Conceptualization, Data curation, Methodology, Supervision, Writing – review & editing. **Yong-Peng Yang:** Supervision, Data curation, DFT calculation, Methodology. **Zhong-Yi Liu:** Supervision, Funding acquisition.

Declaration of Competing Interest

The authors declare that they have no known competing financial interests or personal relationships that could have appeared to influence the work reported in this paper.

Data Availability

The authors do not have permission to share data.

Acknowledgement

This study is supported by Central Plains Science and Technology Innovation Leader Project (Nos. 214200510006). This work was also supported by the Hefei advanced computing center and Supercomputer Centre in Zhengzhou University (Zhengzhou).

Appendix A. Supporting information

Supplementary data associated with this article can be found in the online version at [doi:10.1016/j.apcatb.2023.122402](https://doi.org/10.1016/j.apcatb.2023.122402).

References

- H. Chen, Y.S. Zhou, W. Guo, B.Y. Xia, Emerging two-dimensional nanocatalysts for electrocatalytic hydrogen production, *Chin. Chem. Lett.* 33 (2022) 1831–1840.
- J. Li, L. Wang, H. He, Y. Chen, Z. Gao, N. Ma, B. Wang, L. Zheng, R. Li, Y. Wei, J. Xu, Y. Xu, B. Cheng, Z. Yin, D. Ma, Interface construction of NiCo LDH/NiCoS based on the 2D ultrathin nanosheet towards oxygen evolution reaction, *Nano Res.* 15 (2022) 4986–4995.
- F. Keivanimehr, S. Habibzadeh, A. Baghban, A. Esmaeili, A. Mohaddespour, A. H. Mashhadzadeh, M.R. Ganjali, M.R. Saeb, V. Fierro, A. Celzard, Electrocatalytic hydrogen evolution on the noble metal-free MoS₂/carbon nanotube heterostructure: a theoretical study, *Sci. Rep.* 11 (2021) 3958.
- S. Yang, J.-Y. Zhu, X.-N. Chen, M.-J. Huang, S.-H. Cai, J.-Y. Han, J.-S. Li, Self-supported bimetallic phosphides with artificial heterointerfaces for enhanced electrochemical water splitting, *ACS Appl. Energy Mater.* 304 (2022), 120914.
- C. Duan, L. Wang, J. Liu, Y. Qu, J. Gao, Y. Yang, B. Wang, J. Li, L. Zheng, M. Li, Z. Yin, 3D carbon electrode with hierarchical nanostructure based on NiCoP core-layered double hydroxide shell for supercapacitors and hydrogen evolution, *ChemElectroChem* 8 (2021) 2272–2281.
- H.C. Fu, X.H. Wang, X.H. Chen, Q. Zhang, N.B. Li, H.Q. Luo, Interfacial engineering of Ni(OH)₂ on W₂C for remarkable alkaline hydrogen production, *ACS Appl. Energy Mater.* 301 (2022), 120818.
- Y. Gao, Z. Chen, Y. Zhao, W. Yu, X. Jiang, M. He, Z. Li, T. Ma, Z. Wu, L. Wang, Facile synthesis of MoP-Ru₂P on porous N, P co-doped carbon for efficiently electrocatalytic hydrogen evolution reaction in full pH range, *Appl. Catal. B* 303 (2022), 120879.
- X.H. Chen, X.L. Li, L.L. Wu, H.C. Fu, J. Luo, L. Shen, Q. Zhang, J.L. Lei, H.Q. Luo, N. B. Li, Nb₂O₅-Ni₃N heterojunction tuned by interface oxygen vacancy engineering for the enhancement of electrocatalytic hydrogen evolution activity, *J. Mater. Chem. A* 9 (2021) 11563–11570.
- X. Xu, L. Liu, MoS₂ with controlled thickness for electrocatalytic hydrogen evolution, *Nanoscale Res. Lett.* 16 (2021) 137.
- D. Vikraman, S. Hussain, S.A. Patil, L. Truong, A.A. Arbab, S.H. Jeong, S.H. Chun, J. Jung, H.S. Kim, Engineering MoSe₂/WS₂ hybrids to replace the scarce platinum electrode for hydrogen evolution reactions and dye-sensitized solar cells, *ACS Appl. Mater. Interfaces* 13 (2021) 5061–5072.
- C.-D. Si, Z. Wu, J. Wang, Z.-H. Lu, X. Xu, J.-S. Li, Enhanced the hydrogen evolution performance by Ru nanoparticles doped into cobalt phosphide nanocages, *ACS Sustain. Chem. Eng.* 7 (2019) 9737–9742.
- S. Lv, J. Li, B. Zhang, Y. Shi, X. Liu, T. Wang, In-situ growth of hierarchical CuO@Cu₃P heterostructures with transferable active centers on copper foam substrates as bifunctional electrocatalysts for overall water splitting in alkaline media, *Int. J. Hydrog. Energy* 47 (2022) 9593–9605.
- H. Du, X. Zhang, Q. Tan, R. Kong, F. Qu, Cu₃P-CoP hybrid nanowire array: a superior electrocatalyst for acidic hydrogen evolution reaction, *ChemComm* 53 (2017) 12012–12015.
- A. Manikandan, P. Sriram, K.-C. Hsu, Y.-C. Wang, C.-W. Chen, Y.-C. Shih, T.-J. Yen, H.-T. Jeng, H.-C. Kuo, Y.-L. Chueh, Electrochemically active novel amorphous carbon (a-C)/Cu₃P peapod nanowires by low-temperature chemical vapor phosphorization reaction as high efficient electrocatalysts for hydrogen evolution reaction, *Electrochim. Acta* 318 (2019) 374–383.
- M. Pi, T. Yang, S. Wang, S. Chen, One-pot synthesis of in situ carbon-decorated Cu₃P particles with enhanced electrocatalytic hydrogen evolution performance, *J. Mater. Res.* 33 (2018) 546–555.
- C. Li, J.B. Baek, Recent advances in noble metal (Pt, Ru, and Ir)-based electrocatalysts for efficient hydrogen evolution reaction, *ACS Omega* 5 (2020) 31–40.
- J.J. Ding, D.C. Wu, J.H. Zhu, S.H. Huang, F. Rodriguez-Hernandez, Y. Chen, C. B. Lu, S.Q. Zhou, J.C. Zhang, D. Tranca, X.D. Zhuang, High-entropy carbons: From high-entropy aromatic species to single-atom catalysts for electrocatalysis, *Chem. Eng. J.* 426 (2021), 131320.
- S. Sun, Metallic nanoparticles assembled on graphene as enhanced catalyst for oxygen reduction reaction, *Am. Chem. Soc. Div. Pet. Chem. Prepr.* 58 (2013), 185–185.
- S.-H. Cai, X.-N. Chen, M.-J. Huang, J.-Y. Han, Y.-W. Zhou, J.-S. Li, Interfacial engineering of nickel/iron/ruthenium phosphides for efficient overall water splitting powered by solar energy, *J. Mater. Chem. A* 10 (2022) 772–778.
- C. Zhu, S. Fu, Q. Shi, D. Du, Y. Lin, Single-atom electrocatalysts, *Angew. Chem. Int. Ed. Engl.* 56 (2017) 13944–13960.
- Q. Zhang, J. Guan, Single-atom catalysts for electrocatalytic applications, *Adv. Funct. Mater.* 30 (2020) 2000768.
- Y. Wang, D. Wang, Y. Li, Rational design of single-atom site electrocatalysts: from theoretical understandings to practical applications, *Adv. Mater.* 33 (2021) 2008151.
- Y. Liu, X. Li, Q. Zhang, W. Li, Y. Xie, H. Liu, L. Shang, Z. Liu, Z. Chen, L. Gu, Z. Tang, T. Zhang, S. Lu, A general route to prepare low-ruthenium-content bimetallic electrocatalysts for pH-universal hydrogen evolution reaction by using carbon quantum dots, *Angew. Chem. Int. Ed. Engl.* 59 (2020) 1718–1726.
- J. Zhang, M. Zhang, Y. Zeng, J. Chen, L. Qiu, H. Zhou, C. Sun, Y. Yu, C. Zhu, Z. Zhu, Single Fe atom on hierarchically porous S, N-codoped nanocarbon derived from porphyrin enable boosted oxygen catalysis for rechargeable Zn-Air batteries, *Small* 15 (2019) 1900307.
- M. Liu, R. Zhang, W. Chen, Graphene-supported nanoelectrocatalysts for fuel cells: synthesis, properties, and applications, *Chem. Rev.* 114 (2014) 5117.
- M. Zhang, X. Li, Y. Yang, T. Li, H. Luo, L. Wen, L. Qin, Multilayer self-assemblies for fabricating graphene-supported single-atomic metal via microwave-assisted emulsion micelle, *Small* 18 (2022) 2201291.
- M. Hegazy, M.R. Berber, Y. Yamauchi, A. Pakdel, U.P. Apfel, Synergistic electrocatalytic hydrogen evolution in Ni/NiS nanoparticles wrapped in multi-heteroatom-doped reduced graphene oxide nanosheets, *ACS Appl. Mater. Interfaces* 13 (2021) 34043–34052.
- P. Yin, T. Yao, Y. Wu, L. Zheng, Y. Lin, W. Liu, H. Ju, J. Zhu, X. Hong, Z. Deng, G. Zhou, S. Wei, Y. Li, Single cobalt atoms with precise N-coordination as superior oxygen reduction reaction, *Catal. Angew. Chem. Int. Ed.* 55 (2016) 10800–10805.
- Z. Xu, Y. Zhang, L. Qin, Q. Meng, Z. Xue, L. Qiu, G. Zhang, X. Guo, Q. Li, Crystal facet induced single-atom Pd/Co₂O₃ on a tunable metal-support interface for low temperature catalytic oxidation, *Small* 16 (2020) 2002071.
- D. Yang, P. Li, X.Y. Gao, J. Han, Z.Y. Liu, Y.P. Yang, J.H. Yang, Modulating surface segregation of Ni₂P-Ru₂P/CCG nanoparticles for boosting hydrogen evolution reaction in pH-universal, *Chem. Eng. J.* 432 (2022), 134422.
- Q. He, D. Tian, H. Jiang, D. Cao, S. Wei, D. Liu, P. Song, Y. Lin, L. Song, Achieving efficient alkaline hydrogen evolution reaction over a Ni₅P₄ catalyst incorporating single-atomic Ru sites, *Adv. Mater.* 32 (2020) 1906972.
- Z. Geng, Y. Liu, X. Kong, P. Li, K. Li, Z. Liu, J. Du, M. Shu, R. Si, J. Zeng, Achieving a record-high yield rate of 120.9 μgNH₃ mg cat⁻¹ h⁻¹ for N₂ electrochemical reduction over Ru single-atom catalysts, *Adv. Mater.* 30 (2018) 1803498.
- X. Peng, Y. Mi, S. Zhao, X. Liu, D. Qi, J. Sun, Y. Liu, H. Bao, D. Qu, L. Zhuo, Trifunctional single-atomic Ru sites enable efficient overall water splitting and oxygen reduction in acidic media, *Soc. Sci. Comput. Rev.* 16 (2020) 2002888.
- L. Cao, Q. Luo, J. Chen, L. Wang, Y. Lin, H. Wang, X. Liu, X. Shen, W. Zhang, W. Liu, Z. Qi, Z. Jiang, J. Yang, T. Yao, Dynamic oxygen adsorption on single-atomic Ruthenium catalyst with high performance for acidic oxygen evolution reaction, *Nat. Commun.* 10 (2019) 4849.
- J.Q. Chi, X.Y. Zhang, X. Ma, B. Dong, J.Q. Zhang, B.Y. Guo, M. Yang, L. Wang, Y. M. Chai, C.G. Liu, Interface charge engineering of ultrafine Ru/Ni₃P nanoparticles encapsulated in N,P-codoped hollow carbon nanospheres for efficient hydrogen evolution, *ACS Sustain. Chem. Eng.* 7 (2019) 17714–17722.
- D. Yang, L. Gao, J.H. Yang, New insights into layered graphene materials as substrates to regulate synthesis of Ni-P nanomaterials for electrocatalytic oxidation of methanol and water, *ACS Appl. Mater. Interfaces* 11 (2019) 45189–45198.
- H. Zheng, X. Huang, H. Gao, G. Lu, W. Dong, G. Wang, Cu@Cu₃P core-shell nanowires attached on Ni foam as high-performance electrocatalyst for hydrogen evolution reaction, *Chemistry* 25 (2018) 1083–1089.
- S.T. Wei, K. Qi, Z. Jin, J.S. Cao, W.T. Zheng, H. Chen, X.Q. Cui, One-step synthesis of a self-supported copper phosphide nanobush for overall water splitting, *ACS Omega* 1 (2016) 1367–1373.
- Y. Rong, Y. Ma, F. Guo, J. Qian, H. Li, M. Zhou, Z. Xu, Y.Q. Zheng, T. Li, Paintbrush-like Co doped Cu₃P grown on Cu foam as an efficient janus electrode for overall water splitting, *Int. J. Hydrog. Energy* 44 (2019) 28833–28840.
- P. Jiang, Q. Liu, Y.H. Liang, J.Q. Tian, A.M. Asiri, X.P. Sun, A. Cost-Effective, 3D hydrogen evolution cathode with high catalytic activity: FeP nanowire array as the active phase, *Angew. Chem. Int. Ed.* 53 (2014) 12855–12859.

- [41] P. Liu, J.A. Rodriguez, Catalysts for hydrogen evolution from the NiFe hydrogenase to the Ni₂P(001) surface: the importance of ensemble effect, *J. Am. Chem. Soc.* 127 (2005) 14871–14878.
- [42] C. Pei, M.-C. Kim, Y. Li, C. Xia, J. Kim, W. So, X. Yu, H.S. Park, J.K. Kim, Electron transfer-induced metal spin-crossover at NiCo₂S₄/ReS₂ 2D–2D interfaces for promoting pH-universal hydrogen evolution reaction, *Adv. Funct. Mater.* (2022) 2210072.
- [43] J. Chen, Y. Ha, R. Wang, Y. Liu, H. Xu, B. Shang, R. Wu, H. Pan, Inner Co synergizing outer Ru supported on carbon nanotubes for efficient pH-universal hydrogen evolution, *Catal., Nano-Micro Lett.* 14 (2022) 1–15.
- [44] C.C.W. Kananke-Gamage, F. Ramezanipour, Variation of the electrocatalytic activity of isostructural oxides Sr₂LaFeMnO₇ and Sr₂LaCoMnO₇ for hydrogen and oxygen-evolution reactions, *Dalton Trans.* 50 (2021) 14196–14206.
- [45] W. Cheng, H. Zhang, D. Luan, X.W.D. Lou, Exposing unsaturated Cu₁-O₂ sites in nanoscale Cu-MOF for efficient electrocatalytic hydrogen evolution, *Sci. Adv.* 7 (2021) 2580.
- [46] Y. Yang, Y. Qian, H. Li, Z. Zhang, Y. Mu, D. Do, B. Zhou, J. Dong, W. Yan, Y. Qin, L. Fang, R. Feng, J. Zhou, P. Zhang, J. Dong, G. Yu, Y. Liu, X. Zhang, X. Fan, O-coordinated W-Mo dual-atom catalyst for pH-universal electrocatalytic hydrogen evolution, *Sci. Adv.* 6 (2020) 6586.
- [47] Y. Bai, Y. Li, G. Liu, J. Hu, Assembly of copolymer and metal-organic framework HKUST-1 to form Cu₂-xS/CNFs intertwining network for efficient electrocatalytic hydrogen evolution, *Nanomaterials* 11 (2021) 1505.
- [48] L.X. Peng, L. Su, X. Yu, R.Y. Wang, X.Z. Cui, H. Tian, S.W. Cao, J.L. Shi, B.Y. Xia, Electron redistribution of ruthenium-tungsten oxides Mott-Schottky heterojunction for enhanced hydrogen evolution, *Appl. Catal. B* 308 (2022), 121229.
- [49] J.-S. Li, J.-Y. Li, M.-J. Huang, L.-X. Kong, Z. Wu, Anchoring RuP on 3D hollow graphene nanospheres as efficient and pH-universal electrocatalysts for the hydrogen evolution reaction, *Carbon* 161 (2020) 44–50.
- [50] X. Fan, P. Du, X. Ma, R. Wang, J. Ma, Y. Wang, D. Fan, Y. Long, B. Deng, K. Huang, H. Wu, Mechanochemical synthesis of Pt/Nb₂CTx MXene composites for enhanced electrocatalytic hydrogen evolution, *Materials* 14 (2021) 2426.
- [51] S. Zhao, J. Berry-Gair, W. Li, G. Guan, M. Yang, J. Li, F. Lai, F. Cora, K. Holt, D.J. L. Brett, G. He, I.P. Parkin, The role of phosphate group in doped cobalt molybdate: improved electrocatalytic hydrogen evolution performance, *Adv. Sci.* 7 (2020) 1903674.
- [52] L. Zhang, J. Peng, W. Zhang, Y. Yuan, K. Peng, Rational introduction of borate and phosphate ions on NiCo₂O₄ surface for high-efficiency overall water splitting, *J. Power Sources* 490 (2021), 229541.
- [53] M. Wang, Z. Dang, M. Prato, U. Petralanda, I. Infante, D.V. Shinde, L.D. Trizio, L. Manna, Ruthenium-decorated cobalt selenide nanocrystals for hydrogen, *Evol. ACS Appl. Nano Mater.* 2 (2019) 5695–5703.
- [54] Y. Liu, H. Wang, F. Liu, J. Kang, F. Qiu, C. Ke, Y. Huang, S. Han, F. Zhang, X. Zhuang, Self-assembly approach towards MoS₂-embedded hierarchical porous carbons for enhanced electrocatalytic hydrogen evolution, *Chemistry* 27 (2021) 2155–2164.
- [55] J.-S. Li, S. Zhang, J.Q. Sha, H. Wang, M.Z. Liu, L.X. Kong, G.D. Liu, Confined molybdenum phosphide in p-doped porous carbon as efficient electrocatalysts for hydrogen evolution, *ACS Appl. Mater. Interfaces* 10 (2018) 17140–17146.
- [56] H. Wang, S. Jiao, S. Liu, S. Wang, T. Zhou, Y. Xu, X. Li, Z. Wang, L. Wang, Mesoporous bimetallic Au@Rh core-shell nanowires as efficient electrocatalysts for pH-universal hydrogen evolution, *ACS Appl. Mater. Interfaces* 13 (2021) 30479–30485.
- [57] Y. Feng, W. Feng, J. Wan, J. Chen, H. Wang, S. Li, T. Luo, Y. Hu, C. Yuan, L. Cao, L. Feng, R.W. Jie Li b, J. Huang, Spherical vs. planar: Steering the electronic communication between Ru nanoparticle and single atom to boost the electrocatalytic hydrogen evolution activity both in acid and alkaline, *Appl. Catal. B* 307 (2022), 121193.
- [58] X.H. Chen, H.C. Fu, L.L. Wu, X.L. Li, B. Yang, T. Li, F. Gu, J.L. Lei, N.B. Li, H.Q. Luo, Tuning the d-band center of NiC₂O₄ with Nb₂O₅ to optimize the Volmer step for hydrazine oxidation-assisted hydrogen production, *Green. Chem.* 24 (2022) 5559–5569.
- [59] F. Ma, S. Wang, X. Gong, X. Liu, Z. Wang, P. Wang, Y. Liu, H. Cheng, Y. Dai, Z.Z. a, B. Huang, Highly efficient electrocatalytic hydrogen evolution coupled with upcycling of microplastics in seawater enabled via Ni₃N/W₅N₄ janus nanostructures, *Appl. Catal. B* 307 (2022), 121198.